Presence of surfactants controls the stability of bubble chains in carbonated drinks

Omer Atasi [1],* Mithun Ravisankar [2],* Dominique Legendre [1] and Roberto Zenit [2],†

[1]*Institut de Mécanique des Fluides de Toulouse, Université de Toulouse, CNRS, 31013 Toulouse, France*
[2]*Center for Fluid Mechanics, School of Engineering, Brown University, Providence, Rhode Island 02912, USA*

Bubbles appear when a carbonated drink is poured in a glass. Very stable bubble chains are clearly observed in champagne, showing an almost straight line from microscopic nucleation sites from which they are continuously formed. In some other drinks such as soda, such chains are not straight (not stable). Considering pair interactions for spherical clean bubbles, bubble chains should not be stable, which contradicts these observations. The aim of this work is to explain the conditions for bubble chain stability. For this purpose, experiments and direct numerical simulation are conducted. The bubble size as well as the level of interface contamination are varied to match the range of parameters in typical drinks. Both factors are shown to affect the bubble chain stability. The transition from stable to unstable behavior results from the reversal of the lift force, which is induced by the bubble wake. A criteria based on the production of vorticity at the bubble surface is proposed to identify the conditions of transition from stable to unstable bubble chains. Beyond carbonated drinks, understanding bubble clustering has impact in many two-phase problems of current importance.

I. INTRODUCTION

Flavor and smell are not the only sensorial traits of drinking champagne. The bubble chains that appear in a tall glass complete the trifecta: The beauty and visual satisfaction of observing the consecutive and ordered formation of bubbles are an essential part of the experience. Bubbles in carbonated drinks, not just champagne, form as excess carbon dioxide exsolves from the supersaturated liquid. The supersaturation condition is easily achieved since the bottling pressure is higher than atmospheric, and hence more gas can be dissolved in the liquid. The chains form as bubbles are continuously formed at a certain nucleation site; once the bubble reaches a certain critical size for which buoyancy overcomes the surface tension force that keeps the bubble attached, the bubble begins to ascend freely. Immediately after the bubble has been dislodged, a new one begins to form. This process continues for several minutes until most of the dissolved gas comes out of solution [1]. The speed at which bubble rise in the liquid depends on their size and the liquid properties [2–4]. Once the bubbles reach the liquid surface they briefly remain at it while the liquid film drains [5–9]. When the liquid film becomes sufficiently thin, it spontaneously bursts with a characteristic sound [10] and forms aerosol droplets [9,11,12]. All these processes make a glass of carbonated liquid a complex laboratory of two-phase flows with intricate physicochemical processes [1,11–14].

The present investigation focuses on the stability of bubble chains: As the bubbles form consecutively from the same nucleation site, should they remain in-line or not? Stable in-line motion is

---

*These authors contributed equally to this work.
†Corresponding author: roberto_zenit@brown.edu

commonly observed in champagne and other carbonated wines, but is this what one should expect by considering the hydrodynamic interactions among bubbles? The flow disturbance created by the motion of a single bubble ascending will exert certain influence on a subsequent bubble moving behind. Beyond the curiosity of bubble chains in drinks, these results are important in clarifying the key mechanisms that lead to bubble distributions in bubbly flows in general. The nature of hydrodynamic interactions among bubbles determines whether clusters are formed [15], which, in turn, greatly influences the mixing and agitation levels of bubbly flows [16].

Let us first consider the case of two spherical bubbles, with clean interfaces, rising in-line. If the Reynolds number (defined under Materials and Methods), is higher than 10, then the in-line motion is unstable because bubbles are ejected from the wake of any previous bubble. The process is explained by the wake of the leading bubble. Its interaction with the trailing bubble results in the appearance of a lift force [17,18], F_L:

$$\boldsymbol{F}_L = C_L \rho_l \frac{4\pi R^3}{3} (\mathbf{V}_L - \mathbf{V}_B) \times (\boldsymbol{\nabla} \times \mathbf{V}_L), \tag{1}$$

where $\mathbf{V}_L$ is the velocity field of the leading bubble wake, $\mathbf{V}_B$ is the velocity field of the trailing bubble, and C_L is a lift coefficient (positive) for spherical and clean bubbles. Such unstable in-line bubble interaction has been confirmed by experiments [19] and simulations [18]. Recent simulations have also revealed that the interaction between two bubbles, in the inertial regime, is full of subtleties [20,21].

For the case of bubbles in champagne, and other aqueous carbonated drinks, the bubble Reynolds number increases monotonically after the bubble formation as the bubble continues to grow. However, and most importantly, it reaches a value of Re > 10 a few millimeters after formation [22]. Hence, one would expect that stable bubble chains would not be observed in a glass of champagne. In this investigation we argue that a stable bubble chain is possible only if the lift force acting on the trailing bubble changes sign. In such a case, the bubbles would remain in-line regardless of small disturbances.

Previous investigations have addressed the lift-reversal process. Two mechanisms are known to cause lift reversal, bubble deformation [3,23,24], and surface contamination [25]. Either one, or both, can lead to a reversal of the lift force. Harper [26] envisioned that surfactants were in fact responsible for the stabilization of bubble chains observed on common beverages but did not propose a physical mechanism to explain the stabilization.

The main objective of this work is to clarify the origin of the in-line stabilization of a bubble chain, inspired by the particular case of bubble chains in carbonated drinks. Experiments and numerical simulations are conducted to vary the bubble size and surface contamination independently. To simplify the system, we consider nongrowing bubbles. In the case of carbon dioxide bubbles rising in supersaturated liquids, the bubbles grow as they ascend. Since the grow rate, $\dot{R}$, is smaller than the bubble velocity $\dot{R}/U_B < 1$, the added mass effect can be neglected [22].

II. MATERIALS AND METHODS

A. Relevant dimensionless groups

The problem of a bubble of radius R rising steadily in a fluid of viscosity μ and density ρ under the action of gravity g, with a gas-liquid interfacial tension σ_o, is completely characterized by two nondimensional numbers. We consider here the Bond number and Archimedes number:

$$\text{Bo} = \frac{\rho g R^2}{\sigma_0}, \quad \text{Ar} = \frac{\rho^2 g R^3}{\mu^2}. \tag{2}$$

Note that the Archimedes number is in fact a Reynolds number,

$$\text{Re} = \frac{\rho R U_B}{\mu}, \tag{3}$$

TABLE I. Values of physical properties water (carbonated water, Pellegrino), beer (lager, Tecate) and champagne (sparkling wine, Brut Segura Viudas). The values of the dimensionless numbers were obtained considering bubbles sizes ranging $0.25 < R < 1$ mm.

Fluid	ρ (kg/m^3)	μ (mPa s)	σ (mN/m)	Bo	Ar	La	Ma
Water	998	1.00	72.0	0.008–0.13	152–9726	0–0.1	0.1
Beer	1124	1.36	55.0	0.013–0.20	105–6700	15–38	0.0014
Sparkling wine	1100	1.47	48.0	0.014–0.23	86–5493	0.2–0.7	0.3
Champagne	992	1.44	58.0	0.010–0.17	73–4653	0.2–0.7	0.3

where characteristic velocity $U_B = \rho g R^2 / \mu$ is obtained from the balance of the bubble viscous drag with buoyancy. The bubble deformation can be quantified considering the bubble aspect ratio defined as $\chi = D_L / D_S$, where D_L and D_S are the long and short diameters of an ellipsoidal bubble. It is well known that χ is a function of Bo [27].

The transfer of surfactants is characterized by the bulk and the interface Péclet numbers, respectively defined as:

$$\text{Pe} = \frac{\rho g R^3}{\mu D}, \quad \text{Pe}_s = \frac{\rho g R^3}{\mu D_s}, \tag{4}$$

where D and D_s are the surfactant diffusivity coefficient in the bulk and the bubble surface, respectively. An estimation of Pe$_s$ for an air bubble of millimetric radius inside a liquid containing fatty acids or other long chain surfactants [$D_s \sim O(10^{-10})$] gives Pe$_s \approx 10^8$, indicating negligible surface diffusion. Therefore, D_s has been set to zero in the simulations.

Furthermore, the surfactant presence at the interface introduces three additional nondimensional numbers,

$$\alpha = \frac{k_a C_0 \mu}{\rho g R}, \quad \text{La} = \frac{k_a C_0}{k_d}, \quad \text{and} \quad \text{Ma} = \frac{\mathcal{R} T \Gamma_\infty}{\sigma_0}, \tag{5}$$

namely the solubility parameter α, the Langmuir number La, and the Marangoni number Ma. C_0 is the surfactant concentration in the liquid bulk, Γ_∞ is the maximum concentration of surfactants at the interface, and k_a and k_d are the adsorption and desorption kinetic constants, respectively. $\mathcal{R}$ is the ideal gas constant and T is the absolute temperature. The Langmuir number La compares the adsorption and desorption source terms at the interface. Clean interfaces are observed for La $\to 0$ while saturated interfaces for La $\to \infty$.

The level of rigidity of the interface due to the Marangoni effect can be quantified by comparing the two terms in the right-hand side of Eq. (15), namely the surface tension gradient $\nabla_I \sigma \sim \text{LaMa} \sigma_0 / R$ and the liquid viscous shear $\tau \sim \mu_L U_B / R$ experienced by a noncontaminated bubble. Therefore the "rigidity" parameter Λ [8,28] is

$$\Lambda = \frac{\text{Ma}}{\text{Bo}}. \tag{6}$$

The value of LaΛ increases with interface contamination by surfactants, which in turn result in the increase of the interfacial vorticity as shown in Eq. (16).

B. Range of parameters for bubbly drinks

The density, surface tension, and viscosities for water (Pellegrino sparkling water), a lager beer (Tecate, 4.5% ethanol), sparkling wine (Segura Viudas Brut, 12.5% ethanol), and champagne (Charles de Cazanove, 12% ethanol) were measured using a pycnometer (25 ml), a tensiometer (BPT Mobile, KRUSS Scientific Instruments), and rheometer (ARES-G2 Rheometer, TA instruments, concentric cylinders), respectively. The values of these properties are shown in Table I. These

test beverages were degassed before testing by keeping them in a light vacuum environment (1 mbar) for 1 h.

Considering bubble radii ranging from 0.25 to 1 mm, the expected values of Ar, Bo, and La for beer, champagne, and sparkling water, are summarized in Table I.

To estimate the values of La and Ma for these drinks we considered the type of surfactants and their expected concentrations [29,30]. The equilibrium adsorption parameters for the Langmuir isotherm were determined for various surfactants from equilibrium surface tension measurements.

For champagne, the surfactants are mainly fatty acids that contribute to the organoleptic sensations [11]. For fatty acids, the Langmuir adsorption isotherm was fitted to the equilibrium surface tension measurements, which resulted in 0.02 m^3/mol $< k_a/k_d <$ 0.07 m^3/mol, and $\Gamma_\infty =$ 10^{-5} mol/m^2 [29]. Assuming that $C_0 = 10$ mol/m^3, La ranges from 0.2 to 0.7 and Ma $\approx$ 0.3. Therefore, we estimated that for bubble diameters ranging from 0.25 to 1 mm moving in champagne, the product of the "rigidity parameter" with the Langmuir number is in the range $0.2 <$ LaΛ < 14. The reader is referred to Refs. [31,32] for a more detailed account on the sorption isotherms of small molecules.

For beer most surfactants are proteins of molecular weight ranging from 5 to 100 kDa [33,34]. The adsorption of proteins to air-liquid interfaces is significantly different than the adsorption of small molecules. Most importantly, this adsorption cannot be described by the Langmuir isotherm. Indeed, protein adsorption requires higher activation energy than fatty acids, once adsorbed proteins unfold from their three-dimensional structure and create multilayers of adsorbed proteins conferring elastic and viscous properties to the surface. Also, the adsorption of proteins can be considered as irreversible [30,35,36]. Nevertheless, attempts to fit adsorption isotherms of proteins with the Langmuir isotherm exist. Surface coverage measurements for albumine (molecular weight of 67 kDa) is one example. These measurements gave $k_a/k_d = 1.3 \times 10^4$ m^3/mol and $\Gamma_\infty = 4 \times 10^{-8}$ mol/m^2 [37,38]. Assuming a concentration of surface active proteins ranging from 0.08 to 0.2 g/l [39] and an average molecular weight of 67 kDa, we estimate $0.0012 < C_0 < 0.003$ mol/m^3. Therefore, we obtain Ma ≈ 0.0014 and $15 <$ La < 40. For bubble from 0.25 to 1 mm in radius, we infer La$\Lambda =$ Ma La/Bo ≈ 0.1–1.6. Note that other adsorption isotherms have been derived to describe the adsorption of proteins on air-liquid or liquid-solid interfaces [40,41]; however, the use and implementation of these isotherms is beyond the scope of this study.

Last, for water, we arbitrarily assigned small values of Ma and La to denote that a small amount of surfactants are present due to ordinary laboratory conditions.

C. Experimental setup and materials

Bubble chain experiments were conducted in a rectangular plexiglass tank of $50 \times 50 \times 400$ mm^3. At the bottom of the tank, a needle was inserted through a self-healing rubber stopper. Blunt edge needles of three different inner diameters, d_c, were used to produce bubbles of different sizes (0.16, 0.26, and 1.55 mm). Air was introduced to the needle to produce bubbles using a syringe pump (Harvard Apparatus PHD 2000 series), considering flow rates ranging from 1 to 10 ml/min. The different flow rates resulted in experiments with different bubble formation frequencies which, in turn, resulted in changes in the interbubble spacing.

To match the Archimedes and Bond numbers for bubbles ascending in typical beverages, a mixture of 35–65% (by weight) of water-glycerin was used. The resulting fluid had a viscosity of 0.01 Pa s, which was measured using a rheometer (ARES-G2 Rheometer, TA instruments, concentric cylinders). The properties of the bubbles produced for each capillary are shown in Table II.

To calculate the value of La, we considered that for sodium dodecyl sulfate (SDS) aqueous solutions, $k_a/k_d = 0.11$ m^3/mol, according to Ref. [29]. The critical micellar concentration is 10 mM, approximately; for higher concentrations of SDS, we can consider that the surface concentration no longer increases. Therefore, we assume that $C_\infty = 10$ mM. Therefore, different amount of SDS were added to the fluid to reach values of La relevant to those expected for bubbly drinks.

TABLE II. Experimental conditions. We used four capillaries with inner diameter d_c to produce bubbles of different radius R.

d_c (mm)	R (mm)	Bo	Ar	La
0.16, ○, ●	1.1–1.5	0.18–0.39	155–476	0.0
	0.8–1.0	0.12–0.19	57–115	0.5
	0.8–1.0	0.14–0.20	69–113	1.5
0.26, ○, ●	1.3–1.5	0.26–0.39	262–474	0.0
	1.2–1.3	0.30–0.35	237–292	0.5
	1.3–1.4	0.38–0.44	293–359	1.5
1.55, ○, ●	2.0–2.1	0.63–0.74	993–1243	0.0
	1.8–2.2	0.69–0.94	815–1310	0.5
	1.6–1.9	0.56–0.82	517–908	1.5
0.05, Spark. water, ★	0.25	0.008	152	0.1
0.05, Spark. water, ★	0.64	0.056	2610	0.1
0.06, Spark. water, ★	0.76	0.078	4333	0.1
0.16, Spark. water, ★	0.98	0.128	9042	0.1
0.05, Beer, ☆	0.21	0.009	62	27.5
0.05, Beer, ☆	0.38	0.028	354	27.5
0.06, Beer, ★	0.67	0.089	2015	27.5
0.16, Beer, ★	0.84	0.143	4042	27.5
0.05, Spark. wine, ☆	0.19	0.008	37	0.45
0.06, Spark. wine, ☆	0.59	0.078	1128	0.45
0.16, Spark. wine, ★	0.77	0.133	2507	0.45
0.05, Champagne, ☆	0.39	0.026	276	0.45
0.05, Champagne, ☆	0.52	0.045	654	0.45
0.06, Champagne, ★	0.86	0.125	2985	0.45
0.16, Champagne, ★	0.91	0.139	3506	0.45

A series of experiments were conducted with actual sparkling water, beer, sparkling wine, and real champagne, considering bubble sizes similar to those observed in carbonated liquids. We used a glass capillary that was heated and stretched to have a very small inner diameter where the bubbles were formed. The properties of these liquids appear in Table I and the test conditions are in Table II.

D. Numerical simulations

Direct numerical simulations were conducted with the in-house JADIM code by solving the Navier-Stokes equations coupled with the level-set method. We refer the reader to Refs. [8,42] for a detailed description of the method and its validation. Briefly, Navier-Stokes equations are solved for two Newtonian and incompressible fluids using the finite-volume method (second-order accurate in time and space). Continuity is ensured through a projection method, and the capillary contribution is considered through the classical continuum surface force method [43]. The interface position is tracked using the level-set method where the transport of the signed distance to the interface is controlled through the redistancing method. The important aspect of the considered numerical approach used here is its ability to account for the interface contamination by the presence of surfactant in the liquid bulk. The concentration C of surfactant in the liquid bulk is given by the classical advection-diffusion equation,

$$\frac{\partial C}{\partial t} + \boldsymbol{v_c} \cdot \boldsymbol{\nabla} C = \boldsymbol{\nabla} \cdot (D_c \boldsymbol{\nabla} C), \tag{7}$$

while the surfactant concentration Γ at the interface is given by [44,45]

$$\frac{\partial \Gamma}{\partial t} + \nabla_s \cdot (\mathbf{v_s}\Gamma) = D_s \nabla_s^2 \Gamma + S_\Gamma, \tag{8}$$

where D_c and D_s are the diffusion coefficients of the surfactants in the liquid phase and along the interface, respectively; $\mathbf{v_c}$ is the velocity field in the liquid phase; $\mathbf{v_s}$ is the projection of $\mathbf{v_c}$ on the tangent to the interface; $\nabla_s = [\mathbf{I} - (\mathbf{n} \otimes \mathbf{n})] \cdot \nabla$ is the surface gradient operator; and S_Γ is the adsorption or desorption source term of surfactants at the interface [45,46],

$$S_\Gamma = k_a C_I (\Gamma_\infty - \Gamma) - k_d \Gamma, \tag{9}$$

where k_a and k_d are adsorption and desorption kinetic constants, respectively; Γ_∞ is the maximum concentration of surfactants on the interfaces; and C_I is the surfactant concentration at the vicinity of the gas-liquid interfaces. Considering Eqs. (8) and (9), in a steady state ($S_\Gamma = 0$), the bubble interface is covered by the uniform concentration

$$\Gamma_0 = \Gamma_\infty \frac{\mathrm{La}}{1 + \mathrm{La}}. \tag{10}$$

This concentration is the relevant concentration for the interface concentration normalization [see Eq. (16)].

The variation of the surface tension σ with Γ is described using the Langmuir adsorption isotherm [47]:

$$\sigma = \max\left\{\sigma_\infty, \sigma_0\left[1 + \frac{\mathcal{R}T\Gamma_\infty}{\sigma_0}\ln\left(1 - \frac{\Gamma}{\Gamma_\infty}\right)\right]\right\}, \tag{11}$$

where $\mathcal{R}$ is the ideal gas constant and T is the absolute temperature. σ_∞ is a threshold surface tension, set to $0.05\sigma_0$ for stability purposes. It has been verified that the exact value of this threshold does not affect the bubbles velocity or trajectory and that the surface tension never reaches this threshold for the range of parameter investigated in this study.

III. RESULTS

A. Experiments

To characterize the system we consider millimetric-sized nitrogen bubbles forming in a capillary tube and ascending in different viscous liquids. We vary the Bond, Bo, the Archimedes, Ar, and the Langmuir, La, numbers, defined under Materials and Methods.

Figure 1 shows images of bubble chains (superposing many different instants) using a capillary tube and a clean water-glycerin mixture, considering different gas flow rates. From similitude arguments, the bubble size, liquid properties, and gas flow rate are equivalent to bubbles moving in champagne [48] and other carbonated beverages [49]. In other words, the Archimedes and Bond numbers are matched as closely as possible for this experiments to those of carbonated drinks. The lateral dispersion of bubbles from the point of formation indicates that these chains are not stable. As the gas flow rate increases, the bubble frequency increases and, in turn, the separation distance in between bubbles decreases. The sideways motion of the bubbles appears sooner as the bubble separation decreases. This is expected, since the hydrodynamic interaction is stronger for shorter distances.

To investigate the reason behind the observed unstable behavior of bubble chains we conducted two types of experiments. First, the bubble size was increased considering the same clean fluid by changing the size of the capillary through which the bubbles are produced. These results are shown in Fig. 2(a). In this case, the bubble chain is unstable for small sizes (left and middle images) but transitions to a stable in-line chain behavior for large bubbles (right image). Note that the Bond and Archimedes numbers for these large bubbles are larger than expected for bubble chains in champagne and other beverages (see Materials and Methods).
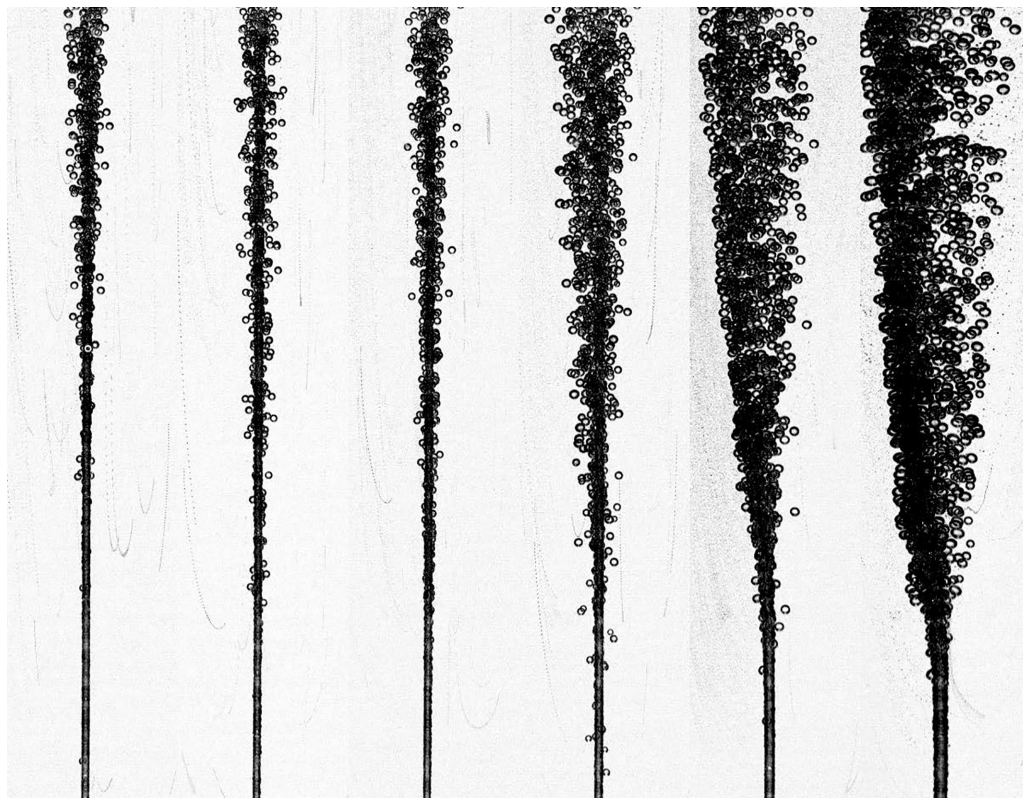
FIG. 1. Bubble chains forming from a capillary in a clean fluid. The flow rate through the capillary increases from 2 to 10 ml/min, from left to right. The bubble frequency ranges from 6 to 18 bubbles/s. Ar ≈ 150, Bo ≈ 0.2, and La = 0 (see the movies in the Supplemental Material [50]).

In the second experiment, we kept the bubble size relatively fixed by using the same capillary tube; hence, Bo and Ar did not change significantly. But in this case, we gradually added a surfactant (sodium dodecyl sulfate) to increase the surface contamination. Figure 2(b) shows that as the amount of surfactants increases, the bubble chains transitions from being unstable to stable. Experiments for only one flow rate are shown for both cases (increasing size and increasing surfactant); experiments for other flow rates (not shown) display the same behavior.

These two experiments clearly indicate that there are two possibilities to stabilize a bubble chain. However, the physical mechanisms that leads to stabilization remains unexplained. To help understand this issue, we conducted numerical simulations.

B. Numerical simulations

The details of the numerical scheme can be found in Sec. II D and in the references cited therein. Most importantly, these simulations are capable of modeling the motion of deformable bubbles considering the presence of surfactants.

The simulations considered a pair of gas bubbles, initially at rest, rising due to buoyancy contained in stagnant fluid domain. To simulate the conditions found in a bubble chain, periodic boundary conditions were imposed on the top and bottom walls of the domain. Many simulations were conducted considering different bubble sizes and contamination levels. The bubble pair is initially placed slightly off the in-line configuration (less the 0.2 R).

(a) R increases, $La \approx 0$ (b) La increases, $R \approx$ constant
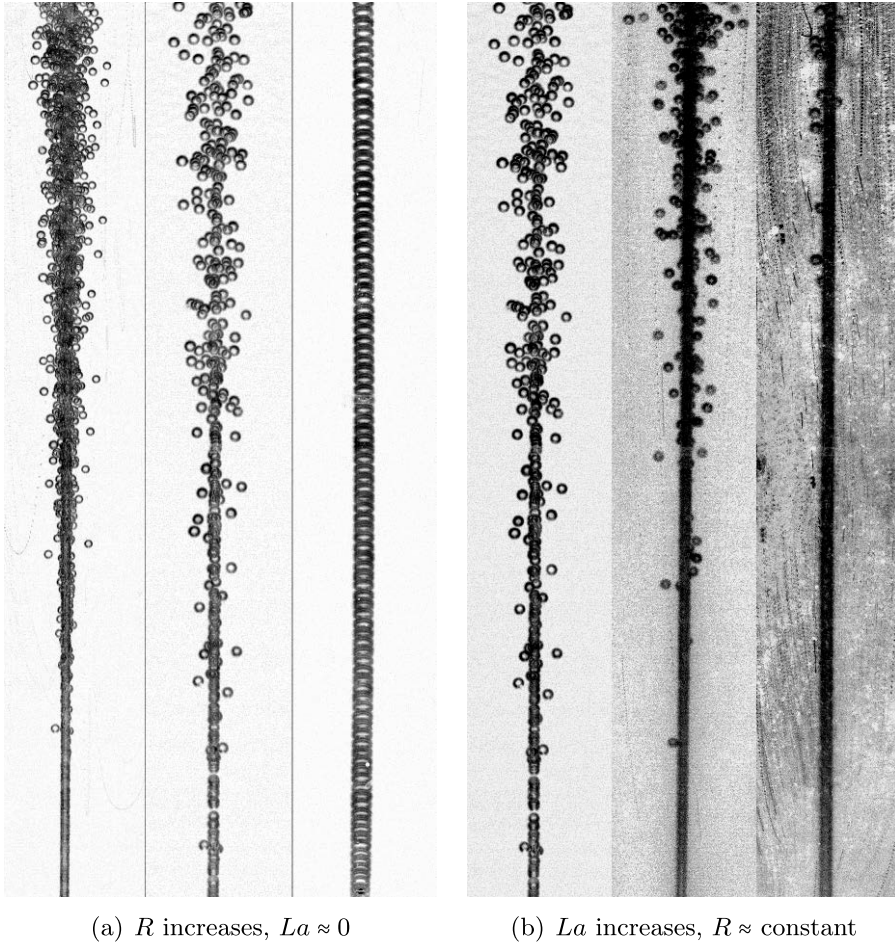
FIG. 2. The effect of bubble size and surface contamination on a bubble chain. (a) The bubble size increases (from left to right) for a liquid without surfactants, La = 0; Ar = (150, 240, 1050), and Bo = (0.18, 0.25, 0.66) for left, center, and right images. (b) The bubble size is approximately the same, but the amount of surfactant increases (from left to right). La = (0, 0.1, 0.5), Ar = (240, 150, 225), and Bo = (0.24, 0.21, 0.32) for left, center, and right images. R is the bubble radius (see the movies in the Supplemental Material [50]).

Figure 3 shows typical results for two characteristic cases. In Figs. 3(a) and 3(b) the results of a nearly spherical bubble pair (Ar = 400) without surfactants (La = 0) are shown. The bubbles start close to an in-line configuration at the start of the simulation; after some time, the bubbles no longer stay vertically aligned, moving away from each other as shown in Fig. 3(a). During this initial transit period, the wake behind the bubbles develops. To visualize the wake, we show isovorticity surfaces of the streamwise vorticity, as shown in Fig. 3(b). The interaction of the bubble with the wake in front of it leads to the appearance of a lift force as indicated by Eq. (1). For the case of spherical bubbles and the absence of surfactants, the wake has two strands of counter-rotating vorticity, in agreement with Ref. [51]. This wake structure induces a lift force in opposite directions for each subsequent bubble. Therefore, the bubbles are pushed sideways, leading to an increasing separation and deviation from the in-line configuration. These chains are unstable.

In contrast, by considering also spherical bubbles (Ar = 400) but including the effect of surfactants such that La = 1 the behavior changes significantly. Figure 3(c) shows the trajectory for the two bubbles. Clearly, the initial in-line configuration remains unchanged even after the initial
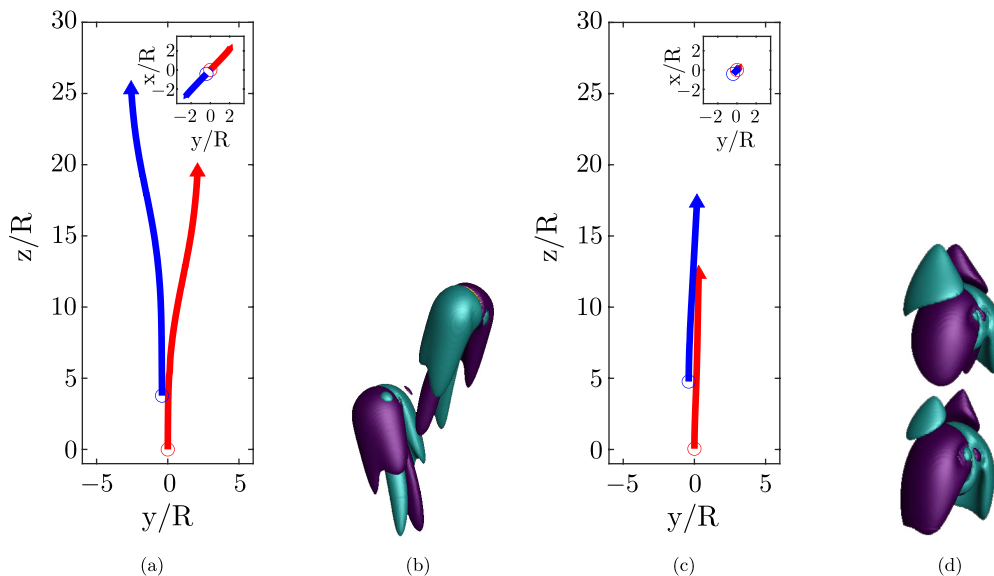
FIG. 3. Simulation of two interacting bubbles ascending in a fluid. [(a) and (c)] The trajectories of the two bubbles, where distances are in bubble radius units; [(b) and (d)] streamwise isovorticity surfaces around the bubbles, $\omega_x U_B/R = \pm 0.05$. For both cases Bo $= 0.05$ and Ar $= 400$; for [(a) and (b)] La $= 0$ and for [(b) and (c)] La $= 1.0$ (see the movies in the Supplemental Material [50]).

transient period. The structure of the wake around the bubbles in this case, shown in Fig. 3(d), is significantly different from the case without surfactants. In particular, the vortex pair developing behind the trailing and leading bubble have the same rotation direction. This configuration induces a lift force of same direction for both bubbles; therefore, the lift force does not destabilize the in-line configuration.

As in the case of experiments, simulations were conducted for varying Ar, Bo, and La to identify the conditions that lead to stability or not. In agreement with the experiments, stable chains were observed for larger bubbles (more deformed) or when surfactants were present. More importantly, since the entire flow field around the bubble pair is known, the vorticity field could be readily obtained. As discussed below, the reversal of the lift force can be attributed to the amount of vorticity created at the bubble surface. Therefore, a criteria for stability can be proposed based on the maximum surface vorticity for each case.

For larger bubbles (for higher Reynolds and Weber numbers), it is well known that the trajectories transitions to a zigzagging path [52]. Although the range of sizes for which such a transition occurs is beyond those occurring in carbonated drinks, a few simulations were also conducted for such large bubbles (not shown here). It was found that the presence of surfactants, the transition to a not-straight path occurs at a smaller value of Reynolds and Weber numbers, in agreement with the experimental observations in Ref. [53].

IV. DISCUSSION

For the range of Bond and Archimedes numbers relevant to bubbly drinks, the in-line clean bubble configuration is unstable. In other words, stable bubble chains cannot be observed because hydrodynamic interactions lead to dispersion. The dispersion is the result of the wake-induced lift force. Increasing the bubble injection frequency increases the lateral dispersion, as shown in Fig. 1. An increase in the bubble frequency results in a smaller separation distance between successive bubbles, for which the wake-induced lift force is larger. Hallez and Legendre [18] showed that the
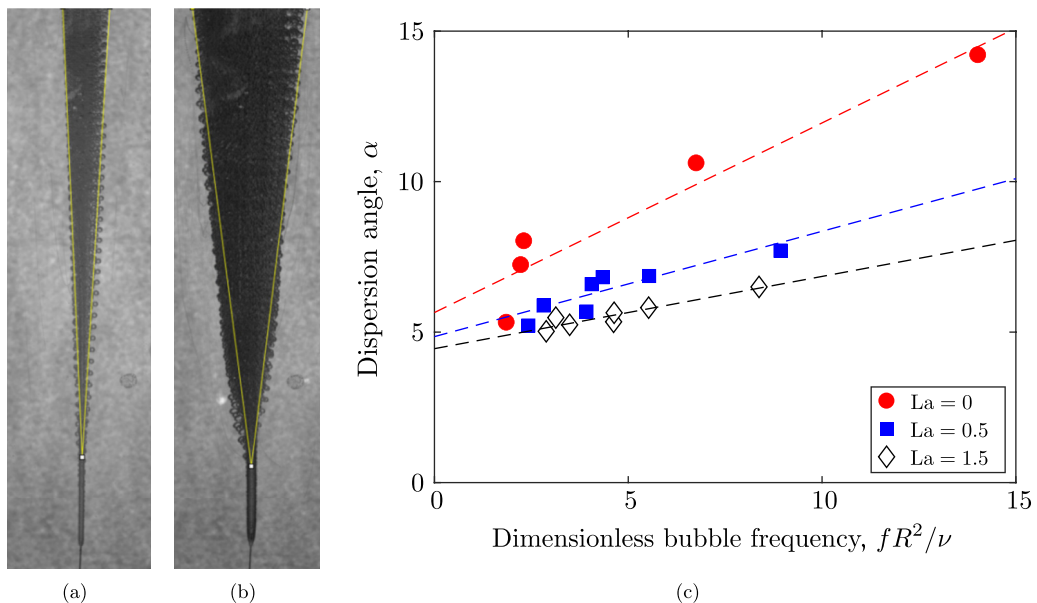
FIG. 4. Dispersion angle of the bubble chain. [(a) and (b)] Images of superposed bubbles over time for the 1 and 10 ml/min, respectively, shown in Fig. 1. In (c), the dispersion angle is shown as a function of the dimensionless bubble frequency, fR^2/ν, for all experiments conducted using the capillary with diameter $d_C = 0.16$ mm.

magnitude of the wake-induced lift is proportional to the rotational part of the wake velocity field; the lift magnitude evolves as $1/[r\sin(\theta)]$ where r is the distance between the two bubbles centers and θ is the angle between the center line and the vertical.

To elaborate further on this idea, we measured the bubble chain dispersion angle, α, for different unstable chains. This is done by superposing the position of bubbles at different instants onto the same frame, as done in Fig. 1 but considering many more bubbles. Figure 4 shows two examples for small and high bubble frequencies, Figs. 1(a) and 1(b), respectively. The angle is calculated by fitting a line from the point at which the chain first becomes unstable to the edge of the bubble cloud on the top of the image, as indicated by the yellow lines in the image. The angle is then plotted as a function of frequency for all experiments, in Fig. 4(c). The plot below shows only the case of small bubbles for different levels of surfactants. The dispersion angle of the unstable bubble chain increases linearly with bubble frequency. This implies that the bubble-bubble distance also influences the instability. Adding surfactants reduces the slope of the trend (the angle increases at a smaller rate with frequency), but the linearity is preserved.

To rationalize this idea we conduct an order of magnitude analysis of the effect of bubble spacing on the induced lift force. From Eq. (1), we can infer that the the lift force, F_L, felt by a trailing bubble evolves as

$$F_L \sim C_L R^3 \frac{U_B^2}{L}\left(1 - \frac{R}{L}\right), \tag{12}$$

where L is the separation distance between bubbles, $L = U_B/f$, where f is the bubble frequency. When C_L has a positive value, the trailing bubble will move sideways at a speed W_B. That motion induces a viscous drag given by $F_D \sim \mu W_B R$. If we balance lift and drag in the horizontal direction (for large values of R/L), we can obtain

$$\alpha \sim \frac{W_B}{U_B} \sim C_L f \frac{R^2}{\nu}, \tag{13}$$

where α is the half-angle of the bubble dispersion of an unstable chain (assuming small α) and ν is the fluid kinematic viscosity. This expression indicates that the angle increases linearly with bubble frequency, in agreement with experimental observations shown in Fig. 4. Furthermore, as surfactants are added C_L is expected to decrease (to eventually reverse, as discussed below), leading to smaller spreading angle. This fact is also in agreement with the experimental measurements.

Interestingly, the dependence of the dispersion angle of bubble chains with bubble frequency resembles behavior of the so-called blooming jets [54]. For such pulsed-jets the angle at which they spread also depends linearly on the pulsating frequency.

The experiments also showed that by increasing the bubble size, without surfactants, a stable bubble chain configuration could be observed, as shown in Fig. 2(a). The bubble chain becomes stable because the lift force changes sign. The origin of the lift reversal for deformed bubbles in a shear flow at large bubble Reynolds number was explained by Adoua et $al.$ [51]. The positive lift effect [$C_L > 0$ in Eq. (1)] results in the tilting and stretching mechanisms of the vorticity of the upstream flow in the bubble wake [17,55]. The vorticity produced at the bubble surface is also tilted and stretched in the wake; however, its contribution gives rise to a streamwise vorticity of opposite sign and thus an induced lift contribution of opposite direction. When the surface vorticity exceeds a certain amount, its contribution becomes dominant and therefore the induced lift changes direction ($C_L < 0$). As the bubble size increases, the bubble shape evolves, becoming more oblate, which, in turn, increases the production of surface vorticity. Hence, it is expected to observe a lift reversal as bubbles become more deformed. Such a change in the lift direction been observed experimentally for air bubbles in different fluids, including water [3,24].

For the case of bubbles in champagne and other carbonated drinks the bubble size is too small to explain the deformation-induced lift reversal. Typically, for a bubble in water, the lift reversal is observed for a bubble Reynolds number Re ≈ 1000 corresponding to a bubble aspect ratio $\chi \approx 2$ [24]. The current experiments and simulations showed that a stable chains could be observed for small spherical bubbles if the surface was contaminated with surfactants. Therefore, we can argue that surfactants can also induce a reversal of the lift force. Such a reversal has been reported in previous experiments [25]. When a sufficient amount of surfactants is present, the bubble surface becomes immobile. In other words, the surface of the bubble can no longer sustain slip. Such nonslip condition leads to an increase of the production of vorticity at the surface which is transported to the bubble wake and is sufficient to change the wake structure. In this case, again, the lift force changes sign, which implies that the trailing bubble in the wake is pushed to remain in-line, forming a stable chain.

Since we have access to all flow properties from the numerical simulations we can calculate the amount of vorticity created at the bubble surface. As discussed above, we expect the surface vorticity to exceed a certain value for increasing bubble deformation, contamination, or both. The magnitude of the vorticity at the bubble surface is calculated for each time step of the simulation. To quantify the vorticity production we consider two quantities: the maximum value or a surface average value. Each of these quantities increases rapidly when the simulations start to quickly reach a steady state value after the initial transient. The time evolution of these two quantities is very similar, varying only in magnitude. We use the maximum value following previous studies [3,56].

The deformation of an air bubble in water can be described in terms of the Bond number, Bo, or the bubble aspect ratio, χ [24,27]. In Fig. 5(a) the maximum value of the surface vorticity for each simulation is shown as a function of the Bond number, Bo, and the bubble aspect ratio, χ. For instance, for a certain bubble size, the Bond number is fixed. By progressively adding surfactants the maximum amount of surface vorticity increases. It is observed that for all cases the bubble pair becomes stable once maximum surface vorticity exceeds a threshold value of $\omega_{\max} R / U_B = 2.65$. This value can be surpassed by adding surfactants or by increasing Bo or χ. The plot also shows that either the aspect ratio or the bubble Bond number can be used to quantify the bubble deformation. We found that the transition could be readily detected by either considering the maximum or mean value of the surface vorticity. The only difference was the value of threshold.
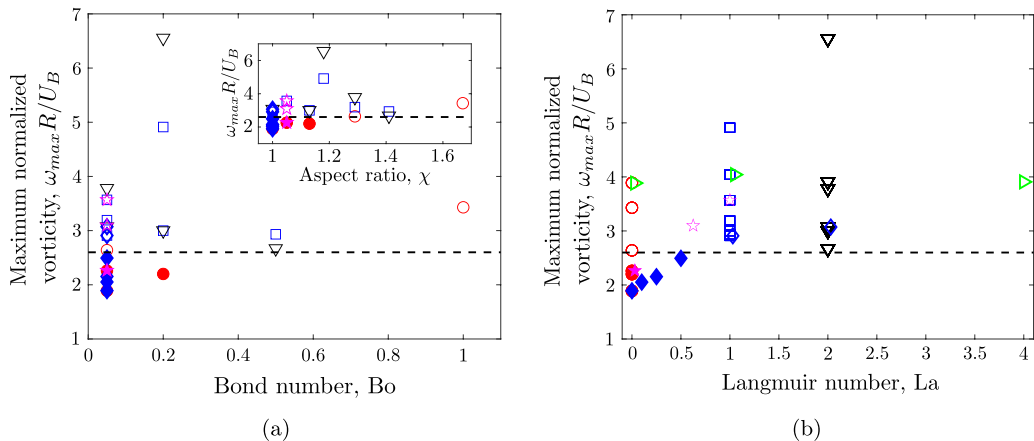
(a)

(b)

FIG. 5. Maximum normalized azimuthal vorticity on bubble surface as function of Bond number (a) and Langmuir number (b). Filled and empty symbols show unstable and stable chains, respectively. The dashed line shows the threshold value of $\omega_{\max} R/U_B = 2.65$. The red circles, blue squares, and black triangles shown simulations for different values of Bo but La $= 0$, La $= 1$, or La $= 2$, respectively. The blue diamonds, magenta stars, and green sideways triangles show simulations for which both Bo and La were varied. Note that the Ar was also varied in the simulations ($400 < $ Ar $< 11\,000$).

Considering now the effect of surfactant at the interface, in Fig. 5(b) the maximum vorticity is shown as a function of the Langmuir number for different values of the Bond number. As in the previous case, it is clear that the bubbles remain in an in-line configuration once the surface vorticity exceeds the threshold value. Note that some additional simulations are shown here were the value of La gradually increased for a fixed Bo (blue diamonds). The results are in good agreement with the rest of the simulations.

Additionally, to further sustain the argument above we projected the value of the surface vorticity onto the bubble surface for a few selected cases, shown in Appendix. The images show that the maximum vorticity is located at the line of maximum curvature for uncontaminated bubbles (La $= 0$) and at the location where the surfactant gradient is highest for contaminated bubbles (La > 0).

As shown above, the threshold value for $\omega_{\max} \sim 2.65\,U_B/R$ is observed at the transition from an unstable to stable bubble line. The same vorticity amount is required to reverse the lift force when either bubble deformation or bubble surface contamination are increased. This confirms that the transition from unstable to stable is related to the reversal of the lift experienced in the wake of bubble.

To understand why this is the case, let us consider the stress balance at the bubble interface. At the bubble surface, the viscous shear stress, $\boldsymbol{\Sigma}$, balances the gradient of surface tension, $\boldsymbol{\nabla}_I \sigma$:

$$\mathbf{n_b} \cdot \boldsymbol{\Sigma} \cdot (\mathbf{I} - \mathbf{n_b n_b}) = -\boldsymbol{\nabla}_I \sigma, \tag{14}$$

where $\mathbf{n_b}$ is the normal vector to the bubble surface and $\boldsymbol{\nabla}_I = (\mathbf{I} - \mathbf{n_b n_b}) \cdot \boldsymbol{\nabla}$ is the surface gradient operator. The gradient of surface tension can be expressed as a function of the surfactant concentration using the Langmuir adsorption isotherm [47]. The tangential viscous shear along the flow direction is $\mu(\partial u_I/\partial r - u_I/R_c)$ and the interfacial azimuthal vorticity is written as $\omega_I = \partial u_I/\partial r + u_I/R_c$, where u_I is the local bubble interfacial velocity and R_c the radius of curvature. The interfacial vorticity can then be directly expressed as a function of the two above-mentioned mechanisms, namely deformation and surface contamination, as

$$\omega_I = 2\frac{u_I}{R_c} + \frac{\mathcal{R}T\Gamma_\infty}{\mu(\Gamma_\infty - \Gamma)}\boldsymbol{\nabla}_I\Gamma. \tag{15}$$
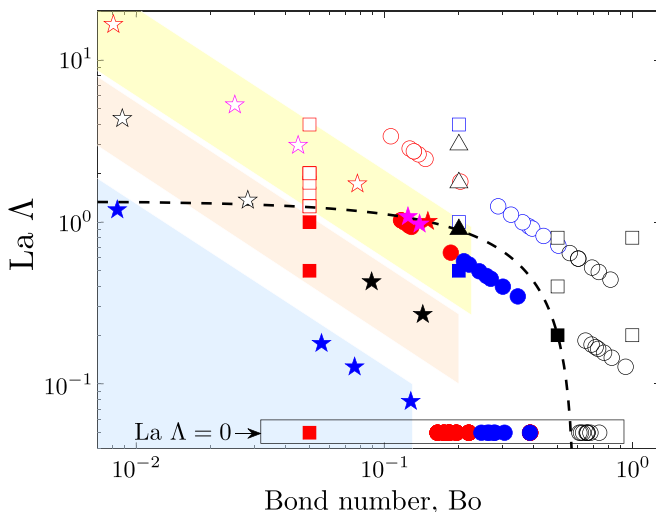
FIG. 6. Stability map showing the stable and unstable chain behavior in terms of the Bond number and the product of the rigidity parameter with the Langmuir number. Filled and empty symbols show unstable and stable chains, respectively. Circles and stars show experimental data, while squares and triangles show numerical results. The data enclosed in the rectangle correspond to cases for $\mathrm{La}\Lambda = 0$ (clean fluids). The dashed line presents an line for which $\omega_{\max}R/U_B \approx 2.65$ which marks the transition. The stars (blue, black, red, and magenta) show the measurements conducted with carbonated water, beer, sparkling wine, and champagne, respectively. The yellow, orange, and blue shaded areas represent the expected range of values for champagne, beer, and water, respectively, according to Table I.

This relation shows that both the surface deformation and the surface contamination can increase the magnitude of the interfacial vorticity, ω_I. Indeed, deformation reduces at the bubble equator the radius of curvature R_c and the surface contamination results in an accumulation of surfactants at the rear of the bubble. This expression can be normalized by considering the bubble equivalent radius R, the characteristic rising velocity of a bubble $\rho g R^2/\mu$, and the concentration of surfactant at equilibrium $\Gamma_0 = \Gamma_\infty \mathrm{La}/(1 + \mathrm{La})$ (see Materials and Methods). The normalized vorticity ω_I^* (denoting all normalized variables with *) at the interface can be written as:

$$\omega_I^* = 2\frac{u_I^*}{R_c^*} + \frac{\mathrm{La}\Lambda}{1 + \mathrm{La}(1 - \Gamma^*)}\boldsymbol{\nabla}_I^*\Gamma^*. \tag{16}$$

With these ideas, we can now propose a stability map that considers both the effect of bubble deformation and surface mobility [the first and second terms in the right-hand side of Eq. (16), respectively] as the main factors determining the stability of a bubble chain. The bubble deformation can be readily quantified by the Bo number. While La quantifies the amount of surfactants that can be transferred from the liquid to the bubble surface, a better measure of the effect of surfactants on the interface behavior is given by the parameter $\mathrm{La}\Lambda$, as demonstrated by Eq. (16).

Figure 6 shows both experiments and simulation results in a map of Bo and $\mathrm{La}\Lambda$. The filled and empty markers show unstable and stable chains, respectively. The combination of bubble deformation and surface rigidity clearly determine the stability conditions of a bubble chain. Furthermore, the transition results from the amount of vorticity created at the bubble surface as indicated by the threshold value (dashed line). If the contamination level and the bubble size are known, the map presented here can be used to determine the stability of a bubble chain. Again, small bubbles, as those typically observed in carbonated drinks, are not expected to be stable in clean liquids. However, the presence of surfactants leads to surface immobilization to result in stable chains.

We can also note that when bubbles are very small, for Ar < 1, a wake will not develop [57] and therefore, regardless of contamination, a lift force does not appear. In aqueous liquids, an Ar < 1 corresponds to Bo $< 10^{-3}$. Bubble chains to the left of this value in the map shown in Fig. 6 will be stable.

In this study, we neglect the effect of bubble growth. Since the growth rate of the bubbles is smaller than the bubbles velocity, the flow field around the bubbles is decoupled from the bubble growth, i.e., at every moment, the flow field is at equilibrium with the bubble size and shape. Therefore, Fig. 6 can be used to predict the evolution of chain stability as the bubbles grow. Indeed, in that situation, Bo and Ar increase as the bubble rise; however, LaΛ decreases as the bubble grows. Therefore, the chain may transition from stable to unstable, and vice versa, as the bubbles grow.

To end and to sustain that these claims are valid for bubbles in typical carbonated drinks, including champagne, we attempt to quantify the Bond number, the rigidity parameters and the Langmuir number for three types of carbonated beverages. We also conduct experiments with actual beverages. The calculation of Bo is straightforward, since the values of density, size, and surface tension are known. For the calculation of Λ and La, on the other hand, some assumptions must be made of the surface absorption and nature of the typical surfactants in these beverages (see Materials and Methods). Considering bubbles ranging in radius from 0.25 to 1 mm, carbonated water is not expected to produce stable chains since a small amount of surfactants is present. The blue shaded area in Fig. 6 shows the range of parameters valid for water. For champagne, the type of surfactants and the quantities are well studied and known. Hence, it is possible to confidently assign the range of expected values of Λ and Bo for the same range of sizes. The yellow shaded region, shown in Fig. 6, clearly indicates that for this beverage stability of bubble chains is expected for small bubbles. This is in agreement with what is typically observed. For the case of beer, on the other hand, we had to make assumptions to infer Λ, since the typical surfactants are very different. We predict that for the same range of bubbles sizes, denoted by the orange-shaded area in the figure, bubble chains can either be stable or not. This observation can be seen in some beer glasses, but more carefully conducted experiments are needed to assess bubble chain stability and to understand how proteins immobilize the surface of bubbles in beer.

The experiments conducted with very small bubbles in water, beer, sparkling wine, and champagne are also shown in Fig. 6, depicted by the stars. Special glass-pulled capillaries were fabricated to produce bubbles in the size range of actual beverages. The sizes and values of the relevant parameters are shown in Table II (a movie is also included in the Supplemental Material [50]). The chains were stable for sparkling wine and champagne, considering small bubbles. Note that in one case, we were able to produce a weakly unstable bubble chain for sparkling wine (Bo $= 0.13$). For beer, the smallest bubble size produced stable chains, while the other two sizes showed unstable chains. For water, experiments with these small bubble sizes were all unstable. These observations are in good agreement with our experiments with mock fluids and numerical simulations.

V. CONCLUSIONS

In summary, we have demonstrated that the stable bubble chains typically observed in champagne occur due to the presence of surfactants. For certain bubble sizes, the bubbles can only move in-line if enough vorticity is produced on their surface. If bubbles are small, then the deformation is not enough to produce sufficient vorticity. Hence, surface immobilization (resulting from the presence of surfactants) provides a second source of vorticity that leads to a stable chain. The current results explain why one observes stable bubble chains in champagne but also provide an interesting case study of sources of vorticity in bubbly two-phase flows. Additionally, since these effects are now identified, the stability of a bubble chain could be used to assess the level of surfactant contamination in any liquid. This idea could be of practical use.
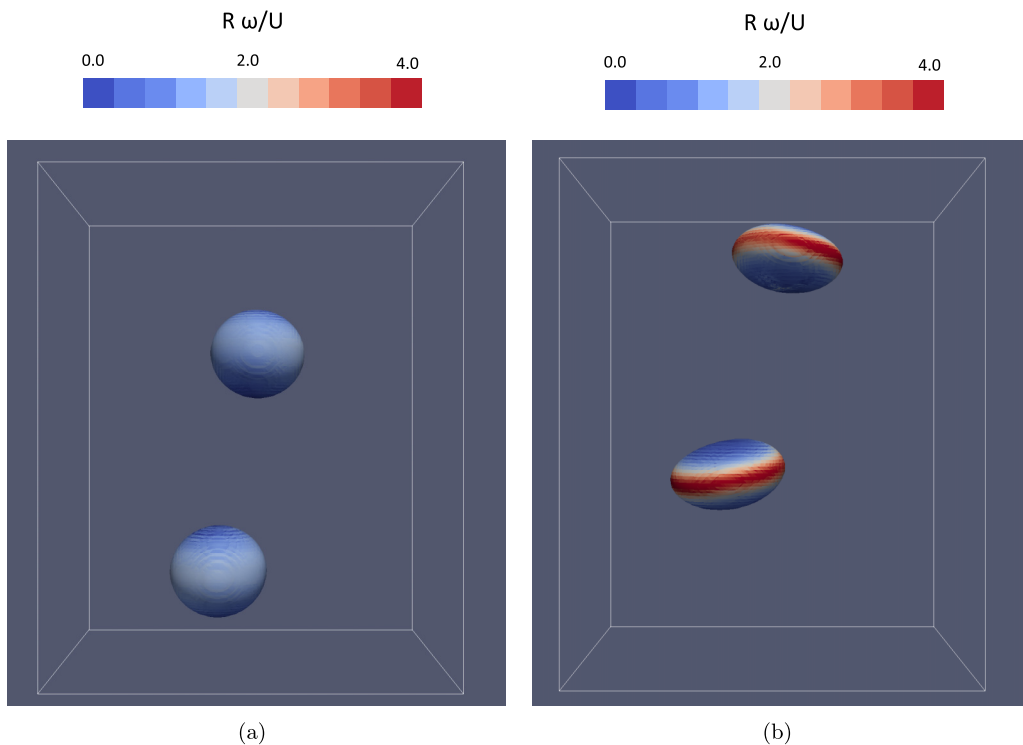
FIG. 7. Map of the normalized azimuthal vorticity on bubble surface for (a) La $= 0$, Bo $= 0.06$, Ar $= 400$ and (b) La $= 0$, Bo $= 0.2$, and Ar $= 11\,000$.

APPENDIX: DISTRIBUTION OF BUBBLE SURFACE VORTICITY

To show how value of vorticity changes over the surface of the bubble, we calculate the magnitude of the azimuthal vorticity and map it onto the bubble surface for several typical cases. Figure 7 shows two cases for uncontaminated bubbles. In both of these cases, the region of highest surface vorticity coincides with the location of highest radius of curvature. In other words, the maximum surface vorticity is located at the bubble equator. As discussed above, the bubble deformation induces the production of surface vorticity. Magnaudet and Mougin [56] calculated the amount of maximum surface vorticity on an oblate bubble, considering an infinitely large Reynolds number. The numerical results shown here are in good agreement with their calculations.

The second important mechanism for the production of surface vorticity is the presence of surfactants, but more specifically the apparance of surface tension gradients. The flow induces a redistribution of surfactants on the bubble surface, which leads to the appearance different values of the surface tension across the surface. These gradients are, in turn, responsible for generating surface vorticity. Since our numerical scheme is capable of capturing the transport of surfactants on the bubble surface, as detailed under Materials and Methods, we can show the location of maximum
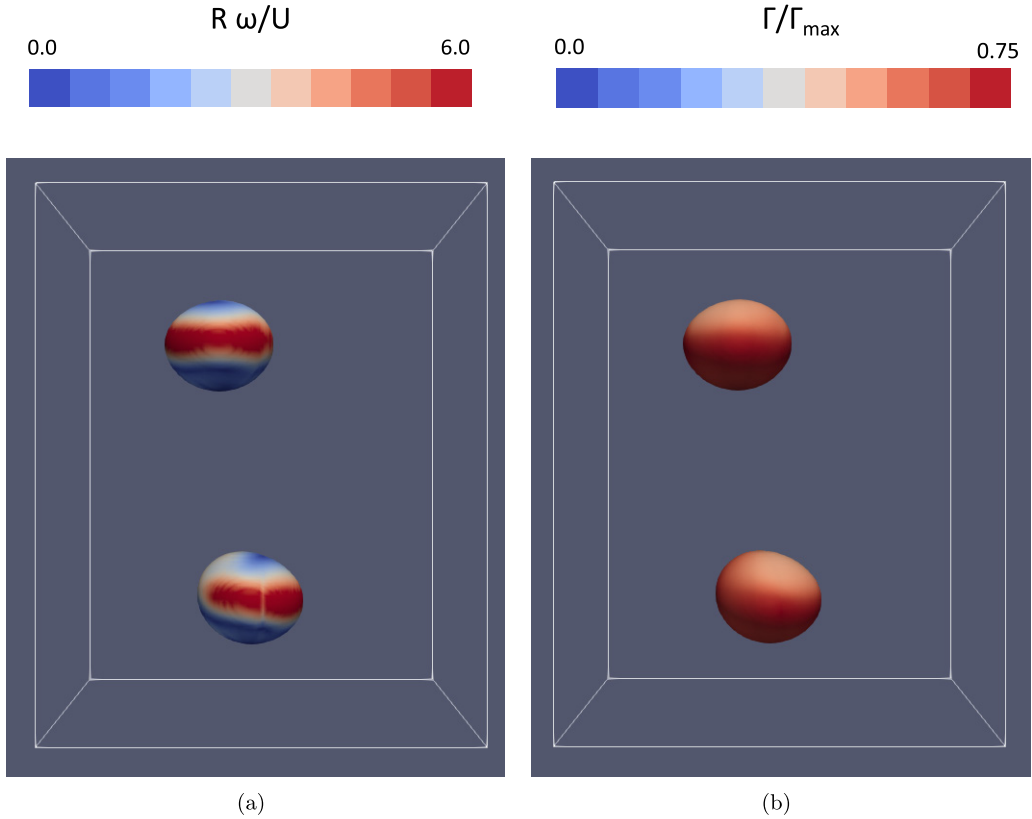
FIG. 8. (a) Map of the normalized azimuthal vorticity on bubble surface for La = 2.0, Bo = 0.2, and Ar = 11 000. (b) The map of normalized surfactant concentration, Γ/Γ_{max}, corresponding to the case in (a).

vorticity changes when surfactants are present. Figure 8(a) shows the map of surface vorticity for a bubble with La = 2.0. The red stripe that denotes the location of maximum vorticity, which has a larger value than the uncontaminated bubble, no longer appears at the bubble equator. Instead, its location is at the region where the surface concentration gradient is highest, as shown in Fig. 8(b). The figure show the surfactant concentration, Γ, mapped onto the bubble surface for the same bubble pair shown in Fig. 8(a). This increased value of the maximum vorticity and its change in location is in agreement with our discussion, see Eq. (16).

[1] G. Liger-Belair, The physics and chemistry behind the bubbling properties of champagne and sparkling wines: A state-of-the-art review, J. Agric. Food Chem. **53**, 2788 (2005).

[2] M. K. Tripathi, K. C. Sahu, and R. Govindarajan, Dynamics of an initially spherical bubble rising in quiescent liquid, Nat. Commun. **6**, 6268 (2015).

[3] K. Hayashi, D. Legendre, and A. Tomiyama, Lift coefficients of clean ellipsoidal bubbles in linear shear flows, Int. J. Multiphase Flow **129**, 103350 (2020).

[4] A. Senapati, G. Singh, and R. Lakkaraju, Numerical simulations of an inline rising unequal-sized bubble pair in a liquid column, Chem. Eng. Sci. **208**, 115159 (2019).

[5] A. Aradian, E. Raphael, and P.-G. de Gennes, Marginal pinching in soap films, Europhys. Lett. **55**, 834 (2001).

[6] H. Lhuissier and E. Villermaux, Bursting bubble aerosols, J. Fluid Mech. **696**, 5 (2012).

[7] L. Champougny, M. Roche, W. Drenckhan, and E. Rio, Life and death of not so bare bubbles, Soft Matter **12**, 5276 (2016).

[8] O. Atasi, B. Haut, A. Pedrono, B. Scheid, and D. Legendre, Influence of soluble surfactants and deformation on the dynamics of centered bubbles in cylindrical microchannels, Langmuir **34**, 10048 (2018).

[9] G. Rage, O. Atasi, M. M. Wilhelmus, J. F. Hernandez-Sanchez, B. Haut, B. Scheid, D. Legendre, and R. Zenit, Bubbles determine the amount of alcohol in Mezcal, Sci. Rep. **10**, 11014 (2020).

[10] M. Poujol, R. Wunenburger, F. Ollivier, A. Antkowiak, and J. Pierre, Sound of effervescence, Phys. Rev. Fluids **6**, 013604 (2021).

[11] G. Liger-Belair, C. Cilindre, R. D. Gougeon, M. Lucio, I. Gebefugi, P. Jeandet, and P. Schmitt-Kopplin, Unraveling different chemical fingerprints between a champagne wine and its aerosols, Proc. Natl. Acad. Sci. USA **106**, 16545 (2009).

[12] E. Ghabache, G. Liger-Belair, A. Antkowiak, and T. Saon, Evaporation of droplets in a champagne wine aerosol, Sci. Rep. **6**, 25148 (2016).

[13] G. Liger-Belair, G. Polidori, and P. Jeandet, Recent advances in the science of champagne bubbles, Chem. Soc. Rev. **37**, 2490 (2008).

[14] R. Zenit and J. Rodriguez-Rodriguez, The fluid mechanics of bubbly drinks, Phys. Today **71**, 44 (2018).

[15] J. R. Vélez-Cordero, J. Lantenet, J. Hernandez-Cordero, and R. Zenit, Compact bubble clusters in newtonian and non-newtonian liquids, Phys. Fluids **26**, 053101 (2014).

[16] F. Risso, Agitation, mixing, and transfers induced by bubbles, Annu. Rev. Fluid Mech. **50**, 25 (2018).

[17] D. Legendre and J. Magnaudet, The lift force on a spherical bubble in a viscous linear shear flow, J. Fluid Mech. **368**, 81 (1998).

[18] Y. Hallez and D. Legendre, Interaction between two spherical bubbles rising in a viscous liquid, J. Fluid Mech. **673**, 406 (2011).

[19] H. Kusuno, H. Yamamoto, and T. Sanada, Lift force acting on a pair of clean bubbles rising in-line, Phys. Fluids **31**, 072105 (2019).

[20] J. Zhang, M.-J. Ni, and J. Magnaudet, Three-dimensional dynamics of a pair of deformable bubbles rising initially in line. Part 1. Moderately inertial regimes, J. Fluid Mech. **920**, A16 (2021).

[21] J. Zhang, M.-J. Ni, and J. Magnaudet, Three-dimensional dynamics of a pair of deformable bubbles rising initially in line. Part 2. Highly inertial regimes, J. Fluid Mech. **943**, A10 (2022).

[22] G. Liger-Belair, R. Marchal, B. Robillard, T. Dambrouck, A. Maujean, M. Vignes-Adler, and P. Jeandet, On the velocity of expanding spherical gas bubbles rising in line in supersaturated hydroalcoholic solutions: Application to bubble trains in carbonated beverages, Langmuir **16**, 1889 (2000).

[23] A. Tomiyama, H. Tamai, I. Zun, and S. Hosokawa, Transverse migration of single bubbles in simple shear flows, Chem. Eng. Sci. **57**, 1849 (2002).

[24] K. Hayashi, H. Hessenkemper, D. Lucas, D. Legendre, and A. Tomiyama, Scaling of lift reversal of deformed bubbles in air-water systems, Int. J. Multiphase Flow **142**, 103653 (2021).

[25] S. Takagi, T. Ogasawara, and Y. Matsumoto, The effects of surfactant on the multiscale structure of bubbly flows, Philos. Trans. Roy. Soc. A **366**, 2117 (2008).

[26] J. F. Harper, Chapter 15–Bubbles rising in line: Champagne, lager, cider, in *Bubbles in Food 2*, edited by G. M. Campbell, M. G. Scanlon, and D. L. Pyle, American Associate of Cereal Chemists International (AACC International Press, 2008), pp. 147–152.

[27] D. Legendre, R. Zenit, and J. R. Velez-Cordero, On the deformation of gas bubbles in liquids, Phys. Fluids **24**, 043303 (2012).

[28] L. Champougny, B. Scheid, F. Restagno, J. Vermant, and E. Rio, Surfactant-induced rigidity of interfaces: a unified approach to free and dip-coated films, Soft Matter **11**, 2758 (2015).

[29] C.-H. Chang and E. I. Franses, Adsorption dynamics of surfactants at the air/water interface: A critical review of mathematical models, data, and mechanisms, Colloids Surf. A **100**, 1 (1995).

[30] R. Z. Guzman, R. G. Carbonell, and P. Kilpatrick, The adsorption of proteins to gas-liquid interfaces, J. Colloid Interface Sci. **114**, 536 (1986).

[31] J. Eastoe and J. S. Dalton, Dynamic surface tension and adsorption mechanisms of surfactants at the air–water interface, Adv. Colloid Interface Sci. **85**, 103 (2000).

[32] Y. He, P. Yazhgur, A. Salonen, and D. Langevin, Adsorption–desorption kinetics of surfactants at liquid surfaces, Adv. Colloid Interface Sci. **222**, 377 (2015).

[33] L. Blasco, M. Viñas, and T. G. Villa, Proteins influencing foam formation in wine and beer: The role of yeast, Int. Microbiol. **14**, 61 (2011).

[34] M. Didier and B. Bénédicte, Soluble proteins of beer, in *Beer in Health and Disease Prevention* (Elsevier, Amsterdam, 2009), pp. 265–271.

[35] A. V. Makievski, V. B. Fainerman, M. Bree, R. Wüstneck, J. Krägel, and R. Miller, Adsorption of proteins at the liquid/air interface, J. Phys. Chem. B **102**, 417 (1998).

[36] J. Li, M. E. Krause, and R. Tu, *Protein Instability at Interfaces during Drug Product Development: Fundamental Understanding, Evaluation, and Mitigation* (Springer, Berlin, 2021).

[37] C. F. Wertz and M. M. Santore, Adsorption and relaxation kinetics of albumin and fibrinogen on hydrophobic surfaces: Single-species and competitive behavior, Langmuir **15**, 8884 (1999).

[38] R. A. Latour, The langmuir isotherm: A commonly applied but misleading approach for the analysis of protein adsorption behavior, J. Biomed. Mater. Res. A **103**, 949 (2015).

[39] C. Niu, Y. Han, J. Wang, F. Zheng, C. Liu, Y. Li, and Q. Li, Malt derived proteins: Effect of protein z on beer foam stability, Food Biosci. **25**, 21 (2018).

[40] R. Miller, E. V. Aksenenko, V. B. Fainerman, and U. Pison, Kinetics of adsorption of globular proteins at liquid/fluid interfaces, Colloids Surf. A **183-185**, 381 (2001).

[41] B. Noskov and A. Mikhailovskaya, Adsorption kinetics of globular proteins and protein/surfactant complexes at the liquid–gas interface, Soft Matter **9**, 9392 (2013).

[42] T. Abadie, J. Aubin, and D. Legendre, On the combined effects of surface tension force calculation and interface advection on spurious currents within Volume of Fluid and Level Set frameworks, J. Comput. Phys. **297**, 611 (2015).

[43] J. Brackbill, D. B. Kothe, and C. Zemach, A continuum method for modeling surface tension, J. Comput. Phys. **100**, 335 (1992).

[44] H. A. Stone, A simple derivation of the time dependent convective-diffusion equation for surfactant transport along a deforming interface, Phys. Fluids **2**, 111 (1990).

[45] B. Cuenot, J. Magnaudet, and B. Spennato, The effects of slightly soluble surfactants on the flow around a spherical bubble, J. Fluid Mech. **339**, 25 (1997).

[46] M. Muradoglu and G. Tryggvason, A front-tracking method for computation of interfacial flows with soluble surfactants, J. Comput. Phys. **227**, 2238 (2008).

[47] V. Levich, *Physicochemical Hydrodynamics* (Prentice Hall, Hoboken, NJ, 1962).

[48] G. Liger-Belair, R. Marchal, B. Robillard, M. Levignes-Adler, A. Maujean, and P. Jeandet, Study of effervescence in a glass of champagne: Frequencies of bubble formation, growth rates, and velocities of rising bubbles, Am. J. Enol. Viticult. **50**, 317 (1999).

[49] G. Liger-Belair, Carbon dioxide in bottled carbonated waters and subsequent bubble nucleation under standard tasting condition, J. Agricult. Food Chem. **67**, 4560 (2019).

[50] See Supplemental Material at http://link.aps.org/supplemental/10.1103/PhysRevFluids.8.053601 for videos of the experiments and simulations.

[51] R. Adoua, D. Legendre, and J. Magnaudet, Reversal of the Lift Force on an Oblate Bubble in a Weakly Viscous Linear Shear Flow, J. Fluid Mech. **628**, 23 (2009).

[52] G. Mougin and J. Magnaudet, Path Instability of a Rising Bubble, Phys. Rev. Lett. **88**, 014502 (2001).

[53] P. C. Duineveld, The rise velocity and shape of bubbles in pure water at high reynolds number, J. Fluid Mech. **292**, 325 (1995).

[54] W. C. Reynolds, D. E. Parekh, P. J. D. Juvet, and M. J. D. Lee, Bifurcating and blooming jets, Annu. Rev. Fluid Mech. **35**, 295 (2003).

[55] T. R. Auton, The lift force on a spherical body in a rotational flow, J. Fluid Mech. **183**, 199 (1987).

[56] J. Magnaudet and G. Mougin, Wake instability of a fixed spheroidal bubble, J. Fluid Mech. **572**, 311 (2007).

[57] R. Clift, J. R. Grace, and M. E. Weber, *Bubbles, Drops, and Particles* (Courier Corporation, New York, 2005).